A New Class of Sky Blue-Emitting Ir(III) Phosphors Assembled Using Fluorine-free Pyridyl Pyrimidine Cyclometalates; Application toward High Performance Sky Blue and White-Emitting...

14 AUTHORS, INCLUDING:

Chih-Hao Chang
Yuan Ze University
70 PUBLICATIONS **1,797** CITATIONS

Yun Chi
National Tsing Hua University
346 PUBLICATIONS **10,874** CITATIONS

A New Class of Sky-Blue-Emitting Ir(III) Phosphors Assembled Using Fluorine-Free Pyridyl Pyrimidine Cyclometalates: Application toward High-Performance Sky-Blue- and White-Emitting OLEDs

Chih-Hao Chang,[*,†] Zih-Jyun Wu,[†] Chuan-Hao Chiu,[†] Yi-Hu Liang,[†] Yu-Shan Tsai,[‡] Jia-Ling Liao,[‡] Yun Chi,[*,‡] Hsi-Ying Hsieh,[§] Ting-Yi Kuo,[⊥] Gene-Hsiang Lee,[⊥] Hsiao-An Pan,[⊥] Pi-Tai Chou,[*,⊥] Jin-Sheng Lin,[∥] and Meu-Rurng Tseng[∥]

[†]Department of Photonics Engineering, Yuan Ze University, Chung-Li 32003, Taiwan

[‡]Department of Chemistry, National Tsing Hua University, Hsinchu 30013, Taiwan

[§]Department of Food Nutrition, Chung Hwa College of Medical Technology, Tainan 71703, Taiwan

[⊥]Department of Chemistry, National Taiwan University, Taipei 10617, Taiwan

[∥]Material and Chemical Research Laboratories, Industrial Technology Research Institute, Hsinchu 31040, Taiwan

ABSTRACT: Two pyrimidine chelates with the pyridin-2-yl group residing at either the 5- or 4-positions are synthesized. These chelates are then utilized in synthesizing of a new class of heteroleptic Ir(III) metal complexes, namely $[Ir(b5ppm)_2(fppz)]$ **(1)**, $[Ir(b5bpm)_2(fppz)]$ **(2)**, $[Ir(b4bpm)_2(fppz)]$ **(3)**, and $[Ir(b5bpm)(fppz)_2]$ **(4)**, for which the abbreviations b5ppm, b5bpm, b4bpm, and fppz represent chelates derived from 2-*t*-butyl-5-(pyridin-2-yl)pyrimidine, 2-*t*-butyl-5-(4-*t*-butylpyridin-2-yl)pyrimidine, 2-*t*-butyl-4-(4-*t*-butylpyridin-2-yl)pyrimidine, and 3-trifluoromethyl-5-(pyridin-2-yl) pyrazole, respectively. The single crystal X-ray structural analyses were executed on **1** to reveal their coordination arrangement around the Ir(III) metal element. The 5-substituted pyrimidine complexes **1**, **2**, and **4** exhibited the first emission peak wavelength (λ_{max}) located in the range 452−457 nm with high quantum yields, whereas the emission of **3** with 4-substituted pyrimidine was red-shifted substantially to longer wavelength with λ_{max} = 535 nm. These photophysical properties were discussed under the basis of computational approaches, particularly the relationship between emission color and the relative position of nitrogen atoms of pyrimidine fragment. For application, organic light-emitting diodes (OLEDs) were also fabricated using **2** and **4** as dopants, attaining the peak external quantum, luminance, and power efficiencies of 17.9% (38.0 cd/A and 35.8 lm/W) and 15.8% (30.6 cd/A and 24.8 lm/W), respectively. Combining sky blue-emitting **2** and red-emitting $[Os(bpftz)_2(PPh_2Me)_2]$ **(5)**, the phosphorescent white OLEDs were demonstrated with stable pure-white emission at CIE coordinate of (0.33, 0.34), and peak luminance efficiency of 35.3 cd/A, power efficiency of 30.4 lm/W, and external quantum efficiency up to 17.3%.

KEYWORDS: *fluorine-free, pyridyl pyrimidine, iridium, sky blue, phosphorescence, white OLEDs*
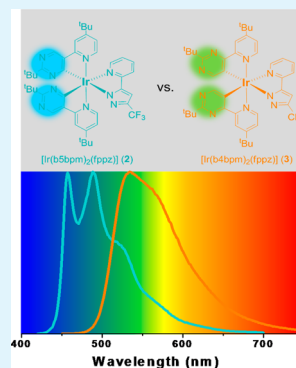
■ INTRODUCTION

Organic light-emitting diodes (OLEDs) have drawn great attention in the past two (plus) decades.[1−17] During the course of development, OLED has gradually evolved from fluorescence to phosphorescence and from monochrome to full-color, which then demands the better designs of red-green-blue (RGB) phosphors for both flat-panel display and solid-state lighting applications. Among them, blue-emitting phosphors are believed to be the critical component because of its highest excitation and emission energy, making blue phosphors the most unstable constituent versus the green and red phosphors.[18,19]

The blue-emitting phosphors are much difficult to prepare among all RGB phosphors.[18,19] The key to the success lies in finding suitable chelates that possess large enough $\pi−\pi^*$ energy gap as well as metal elements with optimal metal-to-ligand charge transfer gap. In addition, these chelates (both chromophoric and ancillary ligands) must have strong metal−ligand bonding interaction so that the *d−d* excited states of the assembled metal complexes or other unspecified quenching states are greatly destabilized to prevent the direct access by thermal activation; the latter would result in a notable reduction in emission efficiencies as well as a decrease in stabilities.

The seminal blue phosphor should be credited to the Ir(III) complex known as FIrpic,[20] for which the central Ir(III) atom is coordinated by two dfppy cyclometalates (dfppyH = 2,4-difluorophenyl pyridine) and one picolinate ancillary. Later on, other structural modifications were routinely conducted, which involved the replacement of either (i) picolinate ancillary or (ii) chromophoric dfppy chelates. Thus, the substitution of picolinate with other L∧X ancillary afforded heteroleptic Ir(III) complexes with general formula $[(dfppy)_2Ir(L∧X)]$, L∧X =

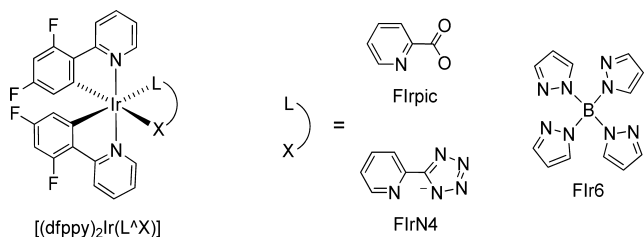*tetra*-pyrazolyl borate in FIr6,[21] and 2-pyridyl tetrazolate in FIrN4.[22,23] (cf. Scheme 1)

Scheme 1. Molecular Structure of Blue Phosphors: FIrpic, FIrN4, and FIr6

The much blue-shifted emission in both FIr6 and FIrN4 can be traced back to the greater electron accepting properties of pyrazolyl borate and pyridyl tetrazolate ancillaries vs that of the picolinate in FIrpic, resulting in the decrease of the electron density at the Ir(III) d_π orbitals, and consequently the reduction of MLCT contribution in the excited states. In recent days, useful design of L∧X ancillary has been even extended to fragments such as 2-pyridyl pyrazolate/triazolate (fppz or fptz),[23] picolinate N-oxide,[24] N,N′-diethyl dithiocarbamate,[25] O,O′-diethyl dithiophosphate,[26] imidodiphosphinate,[27] benzylphosphine,[28−30] and pyrazolylmethyl phosphine,[31] showing the most effective and popular strategy to date for obtaining high-efficiency blue phosphors.

In contrast to the maneuver by varying the ancillary L∧X chelate, the second strategy for achieving blue emission has relied on the decoration of cyclometalate chelates. Suitable designs include: diaryl-1,3,4-oxadiazole,[26] 1-aryl-1,2-pyrazole,[32] imidazole,[33] 5-aryl-1,2,4-triazole,[34] (2,4-difluoro-3-trifluoromethylphenyl)pyridine,[24] (2,4-difluoro-3-cyanophenyl)pyridine,[35] phosphoryl and sulfonyl-substituted 2,4-difluorophenylpyridine,[36] 2′,6′-difluoro-2,3′-bipyridine.[37,38] and 4-aryl-1,2,3-triazole,[39] for which their structural drawings are depicted in Scheme 2 shown below

However, the fluorine substituent on these cyclometalates may impose severe limitation on the device long-term stability. This has been highlighted by a recent study on FIrpic, for which cleavage of fluorine group during OLED operation was confirmed by electron spray ionization mass spectrometry.[40] Furthermore, study on γ-carboline Ir(III) phosphors also showed the regioselective defluorination, which occurred during meridional to facial isomerization.[41] Thus, from the viewpoint of increasing stability, blue-emitting chelate devoid of aromatic fluorine substituent is urgently demanded. We herein describe a new type of such chelate, which is assembled by linking pyrimidinyl and pyridyl groups to form cyclometalate chelates (cf. b5ppmH of Scheme 2). We chose this design as it

could be easily obtained using literature procedures. Moreover, the two nitrogen atoms of pyrimidine would increase its π−π* energy gap to meet the requirement for achieving the designated blue emission.

■ EXPERIMENTAL SECTION

General Procedures. All reactions were performed under nitrogen. Solvents were distilled from appropriate drying agents prior to use. Commercially available reagents were used without further purification. 2-Tri-n-butylstannylpyridine[42] and 4-*t*-butyl-2-tri-n-butylstannylpyridine[43] were prepared according to literature methods, while 4-*t*-butyl-2-acetylpyridine was obtained from direct acetylation of 4-*t*-butylpyridine in presence of FeSO$_4$·7H$_2$O, *p*-acetaldehyde, *t*-BuO$_2$H, and CF$_3$CO$_2$H.[44] All reactions were monitored by TLC with precoated silica gel plates (Merck, 0.20 mm with fluorescent indicator UV254). Compounds were visualized with UV irradiation at 254 or 365 nm. Flash column chromatography was carried out using silica gel obtained from Merck (230−400 mesh). Mass spectra were obtained on a JEOL SX-102A instrument operating in electron impact (EI) or fast atom bombardment (FAB) mode. ¹H and ¹⁹F NMR spectra were recorded on a Bruker-400 or INOVA-500 instrument. Elemental analysis was carried out with a Heraeus CHN-O rapid elementary analyzer.

Preparation of b5ppmH. A mixture of 2-(tri-n-butylstannyl)-pyridine (0.72 g, 1.95 mmol), 5-bromo-2-*t*-butylpyrimidine (0.3 g, 1.39 mmol), and Pd(PPh$_3$)$_4$ (0.11 g, 0.09 mmol) in degassed toluene (25 mL) was refluxed for 24 h under nitrogen. After cooled to RT, CH$_2$Cl$_2$ (50 mL) was added. The organic phase was made basic with addition of NH$_4$OH (5%, 100 mL), followed by washing with water, dried over Na$_2$SO$_4$, filtering and evaporated to dryness. The residue was chromatographed on silica gel with a 1:4 mixture of ethyl acetate and hexane to yield 2-*t*-butyl-5-(pyridin-2-yl)pyrimidine (b5ppmH, 0.27 g, 1.28 mmol, 92%).
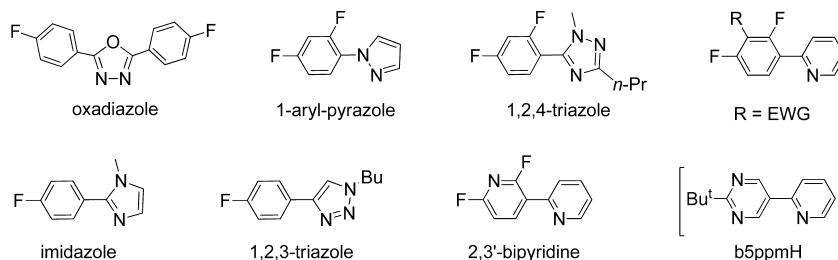
Spectral Data of b5ppmH. ¹H NMR (400 MHz, CDCl$_3$, 294 K): δ 9.23 (s, 2H), 8.71 (d, J_{HH} = 4.8 Hz, 1H), 7.79 (td, J_{HH} = 8.0, 2.0 Hz, 1H), 7.69 (d, J_{HH} = 7.6 Hz, 1H), 7.29 (dd, J_{HH} = 7.6, 4.6 Hz, 1H), 1.41 (s, 9H); MS (EI): *m/z*: 213 [M]⁺.

Preparation of b5bpmH. A mixture of 4-*tert*-butyl-2-tributyl-stannylpyridine (0.83 g, 2.0 mmol) 2-*t*-Butyl-5-bromopyrimidine (0.3 g, 1.4 mmol) and Pd(PPh$_3$)$_4$ (0.11 g, 0.1 mmol) in degassed toluene (20 mL) was refluxed under nitrogen atmosphere for 24 h. After cooling at room temperature, CH$_2$Cl$_2$ (20 mL) was added. The organic phase was made basic with addition of NH$_4$OH (5%, 100 mL), followed by washing with water, dried over Na$_2$SO$_4$, filtering, and evaporated to dryness. The residue was chromatographed on silica gel with a 1:4 mixture of ethyl acetate and hexanes to yield 2-*t*-butyl-5-(4-*t*-butylpyridin-2-yl)pyrimidine (b5bpmH, 0.3 g, 1.11 mmol, 80%).

Spectral Data of b5bpmH. ¹H NMR (400 MHz, CDCl$_3$, 294 K): δ 9.20 (s, 2H), 8.60 (d, J_{HH} = 4.8 Hz, 1H), 7.64 (s, 1H), 7.69 (dd, J_{HH} = 7.6, 2.0 Hz, 1H), 1.44 (s, 9H), 1.34 (s, 9H).

Preparation of (2-pyridinyl)-2-propen-1-one. A mixture of 4-*t*-butyl-2-acetylpyridine (3 g, 16.9 mmol) and N,N-dimethylformamide dimethyl acetal (DMFDMA) (2.16 g, 18.1 mmol) was refluxed for 4.5 h. After cooled down to room temperature, orange-brown solid formed, which was recrystallized from ethyl acetate to yield (E)-1-(4-*t*-

Scheme 2. Structural Drawing of Cyclometalate Chelates with Higher π−π* Energy Gap; EWG = Electron-Withdrawing Group

butylpyridin-2-yl)-3-(dimethylamino)prop-2-en-1-one (3.3 g, 14.21 mmol, 85%).

Spectral Data. ^{1}H NMR: (400 MHz, CDCl$_3$, 294 K): δ 8.51 (d, J_{HH} = 4.8 Hz, 1H), 8.13 (s, 1H), 7.88 (d, J_{HH} = 12.8 Hz, 1H), 7.33 (d, J_{HH} = 6.8 Hz, 1H), 7.42 (d, J_{HH} = 12.8 Hz, 1H), 3.15 (s, 3H), 2.96 (s, 3H), 1.32 (s, 9H).

Preparation of b4bpmH. A mixture of sodium ethoxide (0.44 g, 6.45 mmol) and *t*-butylcarbamidine hydrochloride (0.53 g, 3.87 mmol) in 10 mL of ethanol was stirred at room temperature for 20 min, followed by addition of the previously synthesized prop-2-en-1-one (**L**, 0.5 g, 2.15 mmol). The reaction mixture was then heated up to reflux for 3 h, and then quenched by neutralizing with 2N HCl solution. After drying and removal of solvent, flash chromatography and recrystallization afforded a light yellow 2-*t*-butyl-4-(4-*t*-butylpyridin-2-yl)pyrimidine (b4bpmH, 0.52 g, 1.93 mmol, 90%).

Spectral Data of b4bpmH. ^{1}H NMR: (400 MHz, CDCl$_3$, 294 K): δ 8.78 (d, J_{HH} = 5.2 Hz, 1H), 8.60−8.58 (m, 2H), 8.09 (d, J_{HH} = 5.2 Hz, 1H), 7.36 (d, J_{HH} = 4 Hz, 1H), 1.48 (s, 9H), 1.38 (s, 9H); MS (EI): *m/z*: 269 [M]$^+$.

Preparation of [Ir(b5ppm)$_2$(fppz)] (1). A mixture of b5ppmH (100 mg, 0.28 mmol) and IrCl$_3$·3H$_2$O (100 mg, 0.28 mmol) in 2-methoxyethanol (20 mL) was refluxed for 12 h under N$_2$. It was then cooled to room temperature, followed by the addition of fppzH (0.15g, 1.42 mmol) and Na$_2$CO$_3$ (0.09 g, 4.26 mmol). The resulting mixture was refluxed for another 4 h. After cooled to RT, the solvent was removed under vacuum; the residue was redissolved in 20 mL of ethyl acetate, and this solution was washed with distilled water. The organic phase was dried over Na$_2$SO$_4$, and the solvent was removed in vacuo to yield yellow-brown crude product. Further purification was conducted by silica gel column chromatography using ethyl acetate/hexane (1:1) as the eluent, followed by recrystallization from ethyl acetate and hexane, giving a blue-emitting material [Ir-(b5ppm)$_2$(fppz)] (**1**, 70 mg, 0.08 mmol, 30%).

Spectral Data of 1. ^{1}H NMR (400 MHz, CDCl$_3$, 294 K): δ 8.43 (s, 1H), 8.40 (s, 1H), 7.78−7.65 (m, 9H), 7.08−7.01 (m, 2H), 6.96 (t, J_{HH} = 6.8 Hz, 2H), 1.09 (s, 9H), 1.05 (s, 9H); ^{19}F−{^{1}H} NMR (376 MHz, CDCl$_3$, 294K): δ −60.11 (s, 3F); MS (FAB, ^{193}Ir): *m/z*: 831 [M+2]$^+$; Anal. Calcd for C$_{35}$H$_{33}$F$_3$IrN$_9$: N 15.21, C 50.71, H 4.01. Found: N 14.75, C 50.21, H 4.35.

Selected Crystal Data of 1. C$_{39}$H$_{41}$F$_3$IrN$_9$O$_2$; M = 917.01; triclinic; space group = $P\bar{1}$; *a* = 14.1132(11), *b* = 14.7558(11), *c* = 21.0261(16) Å, α = 74.134(2), β = 73.419(2), γ = 69.258(2)°; *V* = 3851.4(5) Å^3; Z = 4; ρ_{calcd} = 1.581 Mg·m^{-3}; F(000) = 1832; crystal size =0.25 × 0.15 × 0.08 mm^3; λ(Mo−K$_\alpha$) = 0.71073 Å; T = 150(2) K; μ = 3.528 mm^{-1}; 50281 reflections collected, 17626 independent reflections (R$_{int}$ = 0.0555), restraints/parameters =30/996, GOF = 1.092, final R$_1$[$I > 2\sigma(I)$] = 0.0437 and wR_2(all data) = 0.1105.

Preparation of [Ir(b5bpm)$_2$(fppz)] (2). The synthesis follows the procedures described for **1**. For workup, the product was purified by silica gel column chromatography using a 1:3 mixture of ethyl acetate and hexane. Recrystallization from CH$_2$Cl$_2$ and hexanes at RT gives light yellow [Ir(b5bpm)$_2$(fppz)] (**2**, 110 mg, 0.11 mmol, 36%).

Spectral Data of 2. ^{1}H NMR (400 MHz, CDCl$_3$, 294 K): δ 8.40 (s, 1H), 8.39 (s, 1H), 7.76−7.70 (m, 4H), 7.65 (s, 1H), 7.60 (d, J_{HH} = 6.4 Hz, 1H), 7.54 (d, J_{HH} = 6 Hz, 1H), 7.89 (d, J_{HH} = 6 Hz, 1H), 7.03−6.96 (m, 3H), 1.32 (s, 18H), 1.08 (s, 9H), 1.04 (s, 9H); ^{19}F−{^{1}H} NMR (376 MHz, CDCl$_3$, 294K): δ −60.01 (s, 3F); MS (FAB, ^{193}Ir): *m/z*: 943 [M+2]$^+$; Anal. Calcd for C$_{43}$H$_{49}$F$_3$IrN$_9$: N 13.39, C 54.88, H 5.25. Found: N 12.86, C 55.24, H 5.38.

Preparation of [Ir(b4bpm)$_2$(fppz)] (3). The synthesis follows the procedures reported for **1**, and purification was conducted using silica gel column chromatography with ethyl acetate/hexane (1:3) as the eluent. Recrystallization from CH$_2$Cl$_2$ and hexane gives light yellow [Ir(b4bpm)$_2$(fppz)] (**3**, 80 mg, 0.09 mmol, 20%).

Spectral Data of 3. ^{1}H NMR (400 MHz, CDCl$_3$, 294 K): δ 8.50 (d, J_{HH} = 2 Hz, 1H), 8.33 (d, J_{HH} = 2 Hz, 1H), 8.06 (s, 1H), 7.90 (d, J_{HH} = 6 Hz, 1H), 7.84 (s, 1H), 7.64 (d, J_{HH} = 4.8 Hz, 2H), 7.45 (d, J_{HH} = 6 Hz, 1H), 7.39 (d, J_{HH} = 5.6 Hz, 1H), 7.33 (dd, J_{HH} = 8, 2.4 Hz, 1H), 7.33 (dd, J_{HH} = 8, 2.4 Hz, 1H), 7.03 (dd, J_{HH} = 8.4, 2.0 Hz, 1H), 6.95 (s, 1H), 6.86−6.83 (m, 1H), 1.40 (s, 9H), 1.39 (s, 9H), 1.38 (s,

9H), 1.33 (s, 9H); ^{19}F−{^{1}H} NMR (376 MHz, CDCl$_3$, 294K): δ −59.89 (s, 3F); MS (FAB, ^{193}Ir): *m/z*: 943 [M+2]$^+$; Anal. Calcd for C$_{43}$H$_{49}$F$_3$IrN$_9$: N 13.39, C 54.88, H 5.25. Found: N 12.97, C 54.45, H 5.63.

Preparation of [Ir(b5bpm)(fppz)$_2$] (4). A mixture of Ir(tht)$_3$Cl$_3$ (130 mg, 0.23 mmol), b5bpmH (68 mg, 0.25 mmol), and PPh$_3$ (64 mg, 0.24 mmol) in decalin (13 mL) was heated at 180 °C for 6 h. After then, Na$_2$CO$_3$ (122 mg, 1.2 mmol) and fppzH (103 mg, 0.49 mmol) were added, and the mixture was refluxed for another 20 h. Finally, the solvent was evaporated and the residue was eluted by silica gel column chromatography using a 3:2 mixture of hexane and ethyl acetate. Yield: 75 mg, 0.08 mmol, 37%.

Spectral Data of 4. ^{1}H NMR (500 MHz, CDCl$_3$, 294K): 8.48 (s, 1H), 7.84−7.72 (m, 4H), 7.62 (d, J_{HH} = 8 Hz, 1H), 7.55 (d, J_{HH} = 6 Hz, 1H), 7.43 (t, J_{HH} = 6 Hz, 2H), 7.17 (t, J_{HH} = 6.4 Hz, 1H), 7.01−6.98 (m, 2H) 6.88 (s, 1H), 6.86 (s, 1H), 1.33 (s, 9H), 1.07 (s, 9H); ^{19}F−{^{1}H} NMR (376 MHz, CDCl$_3$, 294K): δ −59.75 (s, 3F), −60.02 (s, 3F); MS (FAB, ^{193}Ir): *m/z*: 885 [M]$^+$; Anal. Calcd for C$_{35}$H$_{32}$F$_6$IrN$_9$: N 14.25, C 47.51, H 3.64. Found: N 13.96, C 47.18, H 4.00.

Single-Crystal X-ray Diffraction Studies. Single-crystal X-ray diffraction data were measured on a Bruker SMART Apex CCD diffractometer using Mo radiation (λ = 0.71073 Å). The data collection was executed using the SMART program. Cell refinement and data reduction were performed with the SAINT program. An empirical absorption was applied based on the symmetry-equivalent reflections and the SADABS program. The structures were solved using the SHELXS-97 program and refined using the SHELXL-97 program by full-matrix least-squares on F^2 values. The structural analysis and molecular graphics were obtained using the SHELXTL program on a PC computer.[45]

Photophysical Measurement. Detail of measurement of steady-state absorption and emission in both solution and solid state was described in our previous reports.[46] To determine the phosphorescence quantum yield (Q.Y.) in solution, the samples were degassed by three freeze−pump−thaw cycles. Coumarin 480 (λ_{max} = 473 nm, Q.Y. = 0.87 in methanol) was used as the standard reference for the Q.Y. measurement. Lifetime studies were measured with Edinburgh FL 900 photon-counting system and a hydrogen lamp as the excitation source. Data were fitted by the sum of exponential functions with a temporal resolution of ∼300 ps by using a nonlinear least-squares procedure in combination with an iterative convolution method.

Computational Methodology. Using the density functional theory (DFT) with B3LYP hybrid functional, detail of calculations on electronic singlet and triplet states of all titled complexes has been elaborated in our previous reports.[30,47] In brief, a "double-ζ" quality basis set consisting of Hay and Wadt's effective core potentials (LANL2DZ)[48] was employed for the Ir(III) metal atom, and a 6-31G* basis set, for the rest of atoms. The relativistic effective core potential (ECP) replaced the inner core electrons of Ir(III) metal atom, leaving only the outer core valence electrons (5s^{2}5p^{6}5d^6) to be concerned. Time-dependent DFT (TDDFT) calculations using the B3LYP functional were then performed based on the optimized structures at ground states. Typically, 3 lower triplet and singlet roots of the nonhermitian eigenvalue equations were obtained to determine the vertical excitation energies. Oscillator strengths were then deduced from the dipole transition matrix elements (for singlet states only).

OLED Fabrication. All organics were subject to temperature-gradient sublimation under high vacuum prior to use. OLEDs were fabricated on the indium−tin-oxide (ITO)-coated glass substrates ($\leq$15 Ω) with multiple organic layers sandwiched between the transparent bottom ITO anode and the top metal cathode. Both the organic and metal layers were deposited by thermal evaporation in a vacuum chamber with a base pressure of <10^{-6} Torr. Deposition rate of organics was kept at ∼0.1 nm s^{-1}. The system permitted the fabrication of a complete device in a single pump-down without breaking vacuum. The active area of the device was 2 × 2 mm^2, as defined by the shadow mask for cathode deposition. Current density−voltage−luminance (*J*−*V*−*L*) characterization of the devices was measured using an Agilent 4156C semiconductor parameter analyzer

equipped with a calibrated Si-photodiode. EL spectra of devices were collected by using an Ocean Optics spectrometer.

■ RESULTS AND DISCUSSION

Synthesis. All pyridyl pyrimidine chelates employed in the present studies are synthesized according to the protocols outlined in Scheme 3. On the one hand, the 5-substituted

**Scheme 3. Synthetic Route of the Pyridyl Pyrimidine Chelates[a]**

b5ppmH, R = H
b5bpmH, R = ^tBu

b4bpmH
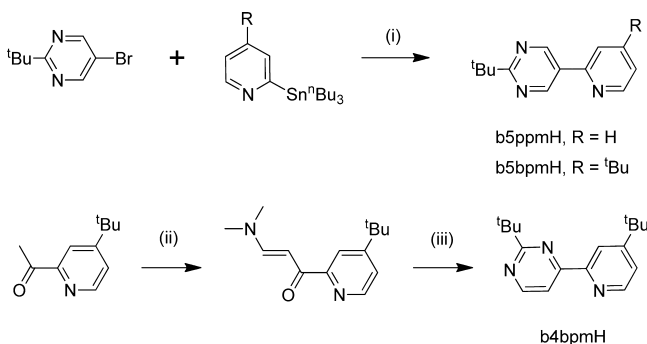
[a]Experimental conditions: (i) Pd(PPh$_3$)$_4$, toluene, reflux; (ii) DMFDMA, 120°C, 4.5 h; (iii) carbamidine hydrochloride, NaOEt, EtOH, reflux, 3 h.

pyridyl pyrimidine, 2-t-butyl-5-(pyridin-2-yl) pyrimidine (b5ppmH) and 2-t-butyl-5-(4-t-butyl-pyridin-2-yl) pyrimidine (b5bpmH), were synthesized under Stille coupling condition using 2-t-butyl-5-bromopyrimidine and 2-(tri-n-butylstannyl)-pyridine or 4-t-butyl-2-(tri-n-butylstannyl)pyridine, respectively. On the other hand, the corresponding 4-substituted, 2-t-butyl-4-(4-t-butylpyridin-2-yl) pyrimidine (b4bpmH) was synthesized by treatment of carbamidine hydrochloride with 3-(dimethylamino)prop-2-en-1-one; the latter was, in turn, obtained in high yield from coupling of 4-t-butyl-2-acetylpyridine and N,N-dimethylformamide dimethyl acetal (DMFDMA) in refluxing ethanol.[49] Despite the seemingly lengthy synthetic procedures for b4bpmH, this chelate was obtained in a much economical manner versus its 5-substituted analogues, b5ppmH and b5bpmH, due to the higher tag price for 2-t-butyl-5-bromopyrimidine. Finally, in all cases, the 2-substituted t-butyl group on pyrimidine is expected to block the coordination capability of the adjacent nitrogen atoms by steric encumbrance, leaving the o-C-H group adjacent to the pyridyl fragment as the dominated reactive center for future chelation to the transition metal atom.

After obtaining the required pyridyl pyrimidine chelates, the respective Ir(III) metal complexes [Ir(b5ppm)$_2$(fppz)] (**1**), [Ir(b5bpm)$_2$(fppz)] (**2**) and [Ir(b4ppm)$_2$(fppz)] (**3**) were synthesized according to the protocols documented in literature. The procedures involved the prior treatment of IrCl$_3$ hydrate with two equiv. of cyclometalate chelate (i.e., b5ppmH, b5bpmH and b4bpmH) in refluxing methoxyethanol solution, followed by addition of 3-trifluoromethyl-5-(2-pyridyl)pyrazole (fppzH) and Na$_2$CO$_3$ as the acid scavenger to the mixture mainly composed of the cyclometalate Ir(III) dimer intermediate.[50−53] In contrast, the complex [Ir(b5bpm)-(fppz)$_2$] (**4**) with dual fppz ancillaries was obtained from treatment of IrCl$_3$·3H$_2$O with stoichiometric amount of b5bpmH and PPh$_3$ in decalin. Without isolation of any intermediate, this reaction was continued by addition of fppzH

and Na$_2$CO$_3$ and vigorous heating according to the established procedures.[54] All isolated products were characterized by FAB mass spectrometry, ^{1}H and ^{19}F NMR spectroscopies, and microanalysis. Their proposed structural drawings are depicted in Scheme 4.

Scheme 4. Structural Drawings of the Studied Ir(III) Complexes 1−4

[Ir(b5ppm)$_2$(fppz)] (**1**)

[Ir(b5bpm)$_2$(fppz)] (**2**)

[Ir(b4bpm)$_2$(fppz)] (**3**)

[Ir(b5bpm)(fppz)$_2$] (**4**)
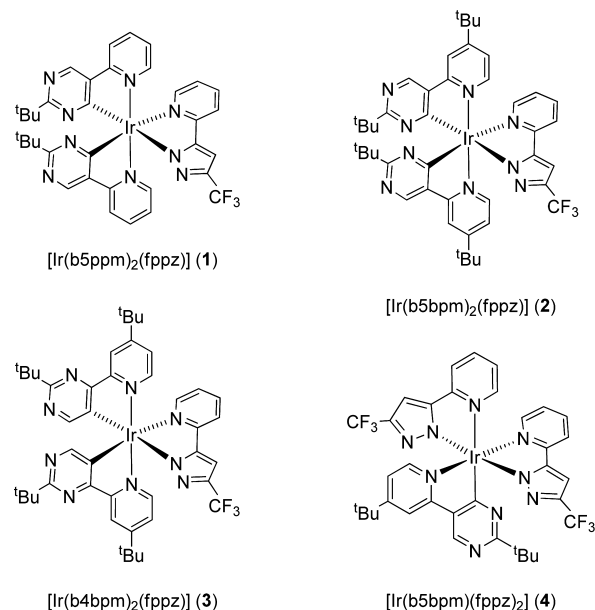
Single-crystal X-ray diffraction studies on **1** was carried out to reveal their exact coordinative arrangement. As indicated in Figure 1, the structure of **1** reveals a slightly distorted
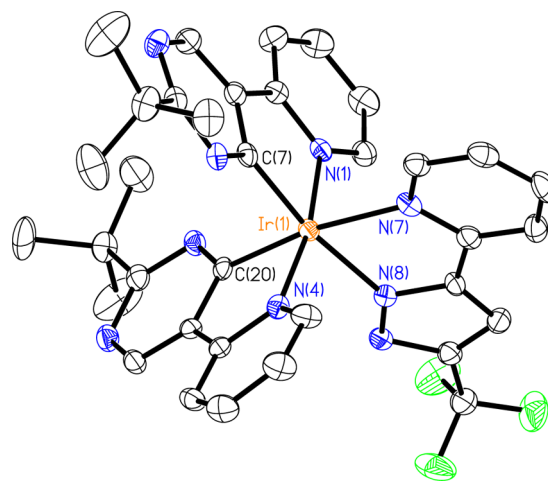
Figure 1. ORTEP diagram of **1** with thermal ellipsoids shown at 40% probability level; selected bond lengths: Ir−C(7) = 1.980(5), Ir−N(4) = 2.052(4), Ir−N(8) = 2.116(4), Ir−C(20) = 1.989(5), Ir−N(1) = 2.052(4), and Ir−N(7) = 2.173(4) Å.

octahedral geometry, similar to the geometry displayed by many heteroleptic Ir(III) complexes.[55−62] The b5ppm ligands show *trans*-Ir-N bond lengths of 2.052(4) and 2.052(4) Å, which are within the normal ranges expected for analogous cyclometalated Ir(III) complexes. The carbon donor atoms C(7) and C(20) are cis to one another, and their respective Ir−C distances, 1.980(5) and 1.989(5) Å, are comparable to those

of the dfppy analogues with ancillary chelates such as [(tfmppy)₂Ir(pic)],[63] [Ir(PyTz)],[64] [Ir(dfpypy)₂(fppz)],[65] and FK306.[66] The metallacycle of the fppz chelate is essentially planar, with the pyrazolate nitrogen atom showing stronger bonding to the metal atom versus the pyridyl donor (cf. Ir–N(8) = 2.116(4) and Ir–N(7) = 2.173(4) Å), which is due to the Coulomb interaction occurring between the Ir(III) metal and negatively charged pyrazolate fragment.

Photophysical Properties. The absorption and luminescence spectra of complexes 1−4 in CH₂Cl₂ are depicted in Figure 2, whereas pertinent numerical data are summarized in
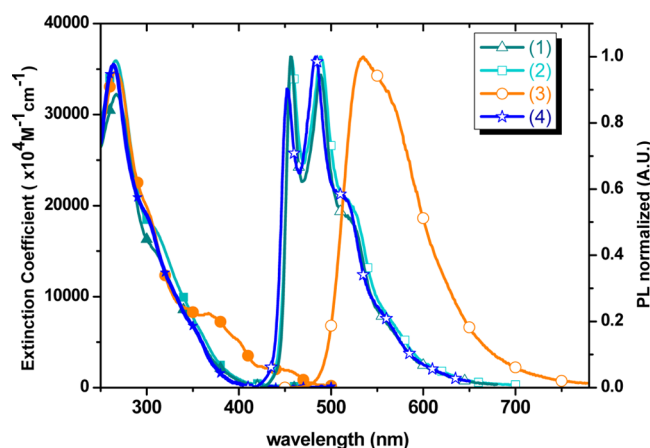
Figure 2. UV/vis absorption and emission spectra of Ir(III) metal complexes in CH₂Cl₂ solution at RT.

Table 1. The strong absorption bands ($\varepsilon > 1 \times 10^4$ M^{-1} cm^{-1}) in the UV region (<350 nm) with distinct vibronic features are assigned to the spin-allowed $^1\pi-\pi^*$ transition of the pyrimidine cyclometalate and pyridyl pyrazolate ligands. The spin-allowed metal to ligand charge-transfer (^{1}MLCT) transition occurs at ∼350−410 nm for the complexes 1, 2, and 4, which is difficult to be resolved due to its mixing with the tail of strong $\pi-\pi^*$ transition. In sharp contrast, complex 3 exhibited substantial red shift of the lower lying transition, with two broad absorption bands observed at 367 and 455 nm, for which the extinction coefficients are in the range 8200 and 1800 M^{-1} cm^{-1}, respectively. The 367 nm band can thus be comfortably assigned to the combination of $^1\pi-\pi^*$ and ^{1}MLCT transitions, whereas the 455 nm absorption may partly originate from spin-forbidden ^{3}MLCT transition that is enhanced by the greater spin−orbit coupling. The well-resolved lower lying absorption bands in 3 manifest the distinct difference of excited-state properties (in terms electronic configuration) between 3 and the family of complexes 1, 2, and 4, which we tentatively

attribute to the dislocation of nitrogen atoms on the pyrimidine cyclometalate, i.e., b4bpmH versus b5bpmH. Details will be elaborated in the following computational section.

Highly intensive luminescence with notable vibronic progressive feature was observed for complexes 1, 2 and 4 in degassed CH₂Cl₂ with first λ_{max} located at 456, 457, and 452 nm, respectively. The entire emission band originating from a triplet state manifold was ascertained by the O₂ quenching rate constant of as high as $(1.5−2.0) \times 10^9$ M^{-1} s^{-1} for all samples. The notable feature of vibronic envelops reminds us that the phosphorescence originates primarily from the $^3\pi-\pi$ state, together perhaps with certain contribution from the ^{3}MLCT excited states. In comparison to 1 possessing the parent pyridyl group, complex 2 bearing the 4-t-butyl substituted pyridyl group should reveal a slightly hypsochromic shift in the emission peak wavelength due to the electron-donating effect of t-butyl substituent, but the actual experimental result showed no such variation. Later computational result also indicates a very slight higher energy shift for 2 (cf. 1), for which the difference may be obscure due to the spectral inhomogeneous broadening in solution. Moreover, complex 4, which is formed by altering one b5bpm cyclometalate to fppz chelate from 2, exhibits a ∼5 nm blue shift (cf. 2) in the first emission peak wavelength. This observation is in accordance with the electron-withdrawing nature of the fppz chelate, which stabilizes the d$_\pi$-orbital energy and hence increases the emission energy. Comparing the family of complexes 1, 2 and 4, which display similar absorption spectra, substantial red-shifted emission with peak wavelength at 535 nm is observed for complex 3. Moreover, in contrast to the structural emission in 1, 2 and 4, the emission of complex 3 relatively lacks the feature of vibronic progression. These emission data all echo the conclusion drawn from the absorption observation, i.e. a distinct difference between 3 and complexes 1, 2, and 4 in the lower lying electronic configuration. Table 1 lists the corresponding photophysical data for the studied complexes in CH₂Cl₂ solution at room temperature. The observed emission lifetimes of ca. 3.67−6.43 μs, together with high quantum yields of 0.49−0.85 in degassed CH₂Cl₂, lead us to deduce the radiative lifetimes of 5.9, 6.4, 7.5, and 10.9 μs for complexes 1−4 in sequence, reconfirming the phosphorescent nature of these Ir(III) samples.

We then performed time-dependent DFT (TD-DFT) calculations in an aim to gain more insight into the fundamental of the associated photophysical properties elaborated above. Figure 3 depicts the selected frontier orbitals involved in the lower-lying transitions of the titled complexes. The vertically excited energy states and their orbital compositions based on the S₀ optimized geometries of the titled complexes are listed in Table 2. As a result, the frontier orbitals of complexes 1 and 2

Table 1. Photophysical Data and Electrochemical Potentials of Complexes 1−4

cpd	UV−vis λ_{max} (nm)[$\varepsilon \times 10^{-3}$]	PL (degassed)			E_{pa}^{ox} (V)^c (LUMO (eV))	E_{pc}^{re} (V)^c (LUMO (eV))
		λ_{max} (nm)^a	QE φ	τ_{obs}^{a}(μs)		
1	267 [32.3], 312 [14.5], 356 [5.6]	456, 488, 521	0.62	3.67	1.04 (−5.84)	−2.75 [irr] (−2.05)
2	267 [36.1], 309 [17.7], 360 [5.8]	457, 489, 521	0.85; 0.60^b	5.47	1.00 (−5.80)	−2.71 [0.13] (−2.09)
3	266 [34.6], 302 [19.3], 367 [8.2], 455 [1.8]	535	0.49	3.67	0.83 (−5.63)	−2.34 [0.11] (−2.46)
4	264 [35.5], 301 [18.8], 352 [6.4]	452, 483, 516	0.59; 0.35^b	6.43	1.13 (−5.93)	−2.70 [irr] (2.1)

^{a}Data recorded in degassed CH₂Cl₂ solution at RT. ^{b}Data recorded in mCP as host material and with a concentration of 6 wt %. $^c E_{pa}^{ox}$ and E_{pc}^{re} were referred to the anodic and cathodic peak potentials referenced to the Fc$^+$/Fc couple in V. The cyclic voltammetry was conducted in either CH₂Cl₂ or THF solution for the oxidation and reduction scans, respectively. The HOMO/LUMO were calculated from the CV data.
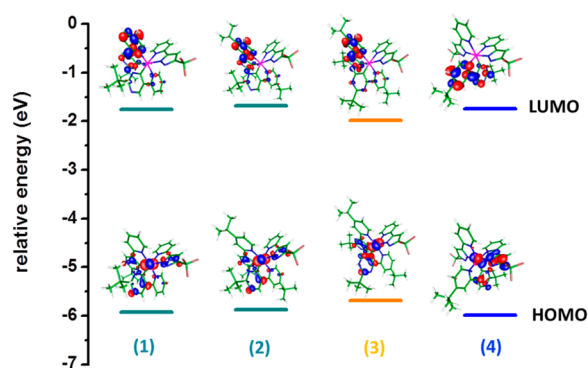
Figure 3. Frontier orbitals involved in the lowest-lying electronic transition for complexes **1−4**. Calculation was done incorporating solvent PCM model in CH₂Cl₂.

Table 2. Computational Energy Levels, Oscillator Strengths, and Orbital Transition Analyses of S₁ and T₁ States for Complexes 1−4 Based on the Optimized Ground State (S₀) Geometry

|	states	λ_{cal} (nm)	f	assignments	MLCT (%)
1	T_1	422.8 (443.3)^a	0	HOMO → LUMO (+37%)	22.47
				HOMO-5 → LUMO+1 (12%)	
	S_1	371.1	0.0172	HOMO → LUMO (+71%)	25.49
2	T_1	422.6 (440.2)^a	0	HOMO → LUMO (+39%)	23.56
				HOMO-5 → LUMO+1 (+9%)	
	S_1	368.1	0.0236	HOMO → LUMO (+72%)	26.57
3	T_1	467.7 (510.2)^a	0	HOMO → LUMO (+81%)	33.89
				HOMO-4 → LUMO+1 (7%)	
	S_1	414.3	0.0482	HOMO → LUMO (+93%)	38.98
4	T_1	418.3 (436.2)^a	0	HOMO → LUMO (+41%)	19.24
				HOMO-5 → LUMO (+26%)	
	S_1	365.4	0.0125	HOMO → LUMO (+45%)	18.44

^{a}The value was obtained via the geometry optimization along the triplet state potential energy surface (PES) followed by the vertical $T_1 \rightarrow S_0$ transition.

are nearly identical, in which the HOMO locates on the pyrazolate of the fppz and in part on the pyrimidine moiety of b5ppm (or b5bpm), whereas the LUMO locates mainly on the pyridyl moiety of b5ppm (or b5bpm). Interesting, different from numerous blue Ir(III) complexes incorporating fppz in which the LUMO resides on the pyridine ring of cyclomatalate, the pyridyl moiety in fppz is no longer where the LUMO locates. This discrepancy can be rationalized by further lowering the π^* energy of the pyridyl moiety in the cyclometalate imposed by the strong electron withdrawing effect from pyrimidine. Due to the same ligand chromophore, a similar mechanism adopted in **1** and **2** should be operative for **4**; however, in **4**, the dual fppz chelates with electron-withdrawing nature are expected to further stabilize the d_π-orbital energy and hence increases the emission energy.

Accordingly, as listed in Table 2, the calculated energy gap is in the order of **1−2 < 4** in both singlet and triplet manifolds, which is also consistent with that deduced from the emission spectra (vide supra).

For complex **3**, the calculated $S_0 \rightarrow S_1$ energy gap is >9 kcal/mol smaller than that of **1**, **2**, and **4**. Careful analysis of the associated frontier orbitals indicates that HOMO of **3** solely resides on the pyrimidine moiety of b4bpmH rather than the residence on both pyrazolate (fppz) and pyrimidine moieties in **1**, **2**, and **4**. In theory, except for the similar electron inductive effect, difference of the pyrimidine between b5bpm and b4bpm lies in that the nitrogen atoms in pyrimidine of b4bpm impose a resonance effect, elongating the π conjugation. The net result causes the upward shifting of pyrimidine π energy level, which then solely contributes to HOMO. Likewise, the consequence of resonance also decreases the π^* energy of pyridyl moiety in b4bpm where LUMO locates, resulting in a substantial decrease of the HOMO−LUMO energy gap in complex **3**. Finally, to more accurately account for the phosphorescence spectra of these complexes, we made further attempts to locate the T_1 state by performing the geometry optimization along the triplet state potential energy surface (PES) for complexes **1−4**, and then executing the vertical $T_1 \rightarrow S_0$ transition to simulate the phosphorescence. As shown in Table 2, the calculated energy in terms of wavelength matches very well with the onset of the phosphorescence.

Electrochemistry. The electrochemical behavior of these Ir(III) metal complexes was investigated by cyclic voltammetry using ferrocene as the internal standard. The results are displayed in Figure 4, with the respective redox data also listed
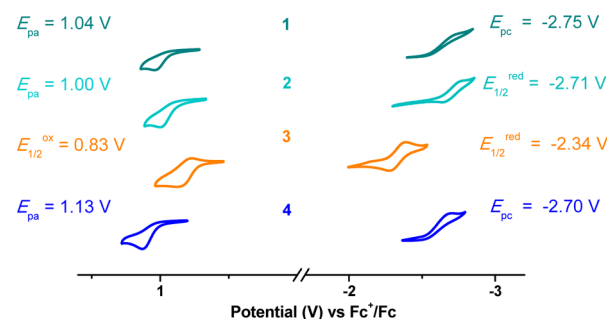
Figure 4. Cyclic voltamograms of Ir(III) metal complexes **1−4**.

in Table 1. During the anodic scan in CH₂Cl₂, all Ir(III) metal complexes exhibited a reversible oxidation with potentials in the region 0.82−1.13 V. Upon the switch to the cathodic sweep in THF, a reversible (or quasi-reversible) reduction with potential ranging from −2.34 to −2.75 V was clearly detected. As revealed previously by electrochemical studies and theoretical calculations in relevant systems,[67−71] the oxidation mainly occurred at the Ir(III) metal site, together with a minor contribution from the cyclometalate chelate, whereas the reduction took place at the electron-accepting portion of the cyclometalate chelate. This assignment is also consistent with the conclusion made in the above computational approach. Accordingly, complexes **1** and **2** should possess very similar electrochemical data, except for the minor influence imposed by the *t*-butyl substituent on cyclometalates. Moreover, complex **4** possesses one additional electron-withdrawing fppz ancillary versus that of **2**, and is thus expected to exhibit a greater (i.e., more positive) oxidation potential compared with that of **2**, while little influence is expected to occur at the

reduction potential, as the fppz ancillaries should not exert the strong influence to the π^*-orbital of the b5bpm cyclometalate. As for the isomeric complex **3**, which displays a much bathochromic emission profile versus all other samples, the reversible oxidation and reduction peaks occur at 0.83 and −2.34 V, for which the much reduced difference in potentials is fully consistent with the associated spectroscopic properties.

OLED Device Fabrication. These new iridium complexes were purified by the temperature-gradient sublimation under high vacuum ambient before use. The sublimation temperature of these new iridium complexes were about 235 °C, which are similar to those of commonly used iridium complexes. Moreover, about 85% recycling rate of all complexes observed evidence the thermal stability of these complexes.

Because of the higher photoluminescence quantum efficiencies of complexes **2** and **4**, both were selected as the dopants to examine the potential of blue phosphorescent OLEDs. On the basis of our previous experience in developing true-blue phosphorescent OLEDs,[28,72−75] their performance is dependent on the effective host−guest energy transfer together with good exciton confinement. In addition, the exciton formation zone should be set further away from the cathode, because the diffused high-energy exciton will be quenched by the surface-plasma of metal.[76] Thus, after considering these design criteria, we selected double emitting layers (DEMLs) and double exciton confining layers (DECLs) to construct the basic framework.

Given the higher triplet energy gaps of both Ir(III) phosphors **2** and **4**, two wide triplet-energy-gap host materials, 3-bis(9-carbazolyl)benzene (mCP)[77,78] and *p*-bis-(triphenylsilyl) benzene (UGH2),[79,80] were selected as the host materials because of their successful application in blue phosphorescent OLEDs. The respective triplet energy gaps (E_T) of mCP and UGH2 are reported to be 2.9 and 3.18 eV. The hole and electron mobilities of mCP are 1.2×10^{-4} and 3.4×10^{-5} cm^2/(V s); thus, it could be roughly categorized as the bipolar host.[81] On the other hand, UGH2 is also known for its better electron-transporting characteristics, which make it useful as the host in deep-blue or true-blue phosphors.[82] Therefore, mCP and UGH2 should be suitable for serving as the main emitting layer EML1 and the secondary emitting layer EML2, respectively. Moreover, the huge difference between the ionization potentials of mCP and UGH2 will form a steep barrier at the mCP/UGH2 interface for boosting the carrier recombination.

Alternatively, di-[4-(*N,N*-ditolyl-amino)-phenyl] cyclohexane (TAPC)[83,84] and 1,3,5-tri[(3-pyridyl)-phen-3-yl]benzene (TmPyPB)[85,86] were selected as the hole-transport layer and electron-transport layer due to their excellent carrier transport capabilities. The respective hole and electron mobilities of TAPC and TmPyPB are about 1×10^{-2} and 1×10^{-3} cm^2/(V s), and both possess large triplet gaps (E_T) of about 2.87 and 2.78 eV, facilitating high energy exciton confinement. As such, we proceeded to construct the device using an configuration of ITO (110 nm)/TAPC (30 nm)/mCP (3 nm)/mCP doped with 6.0 wt % **2** or **4** (25 nm)/UGH2 doped with 6.0 wt % **2** or **4** (3 nm)/UGH2 (2 nm)/TmPyPB (50 nm)/LiF (0.8 nm)/Al (150 nm). The nondoped mCP and UGH2 shown here are exciton confining layers (ECLs). The emitter-doped mCP and UGH2 layers sandwiched between the intrinsic ECLs can restrain the high-energy excitons from migration or diffusion to the adjacent carrier transport layers.[87,88] The blue phosphorescent OLEDs using phosphors **2** and **4** as dopants were named

devices A and B, respectively. A structural drawing of the materials is shown in Scheme 5, while the schematic device structures and energy level diagram of the tested OLEDs are shown in Figure 5.

Scheme 5. Structural Drawings of the OLED Materials Employed in This Study

TAPC

[Os(bpftz)₂(PPh₂Me)] (**5**)

mCP

UGH2

TmPyPB
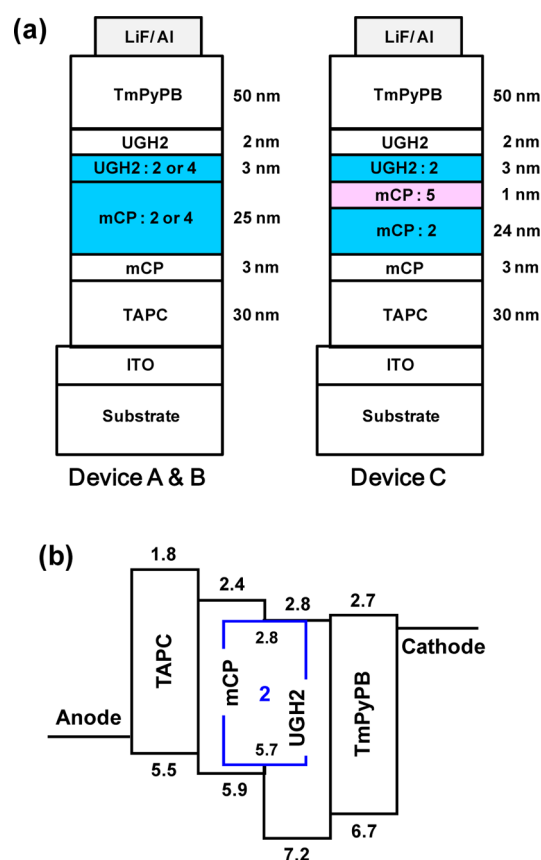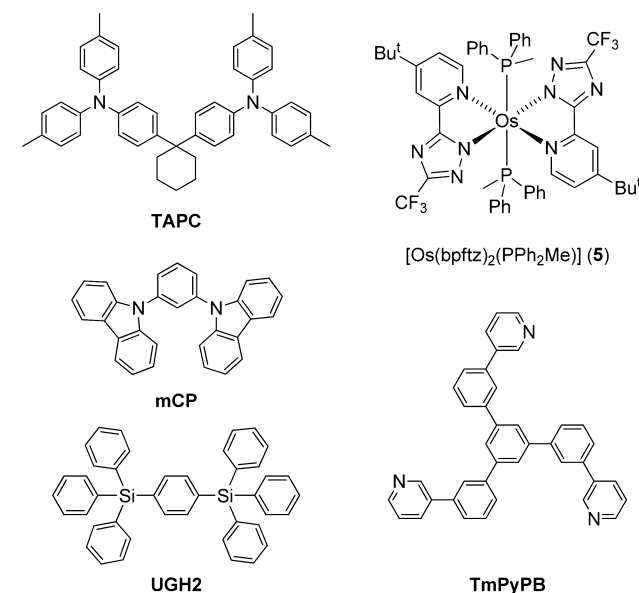
Figure 5. (a) Schematic structures and (b) energy level diagram of the OLED devices. The ³LUMO of **2** is evaluated by the formula: ³LUMO = HOMO − ³Energy gap.

7347

dx.doi.org/10.1021/am401694s | *ACS Appl. Mater. Interfaces* 2013, 5, 7341−7351
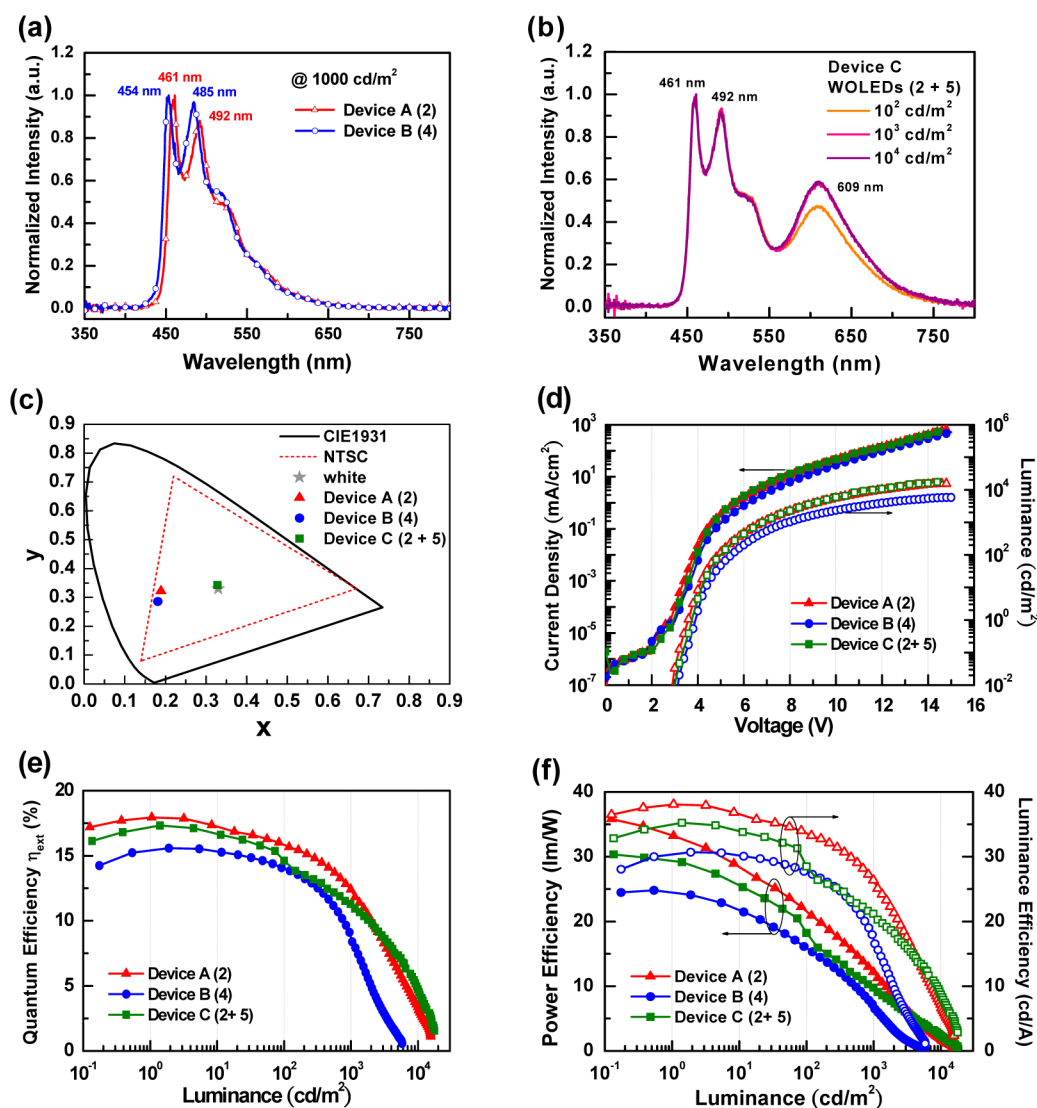
Figure 6. (a) EL spectra of devices A and B, (b) EL spectra of device C at different luminance levels, (c) CIE coordinates, (d) current density–voltage-luminance ($J-V-L$) characteristics, (e) external quantum efficiency vs. luminance, (f) power efficiencies/luminance efficiencies vs. luminance for devices A, B, and C.

Table 3. EL Characteristics of OLEDs with Ir(III) Dopants 2 and 4 and Os(II) Dopant 5

device dopant		A 2	B 4	C (WOLED) 2 + 5
external quantum efficiency (%)	a	17.9	15.5	17.3
	b	15.8	14.0	14.6
luminescence efficiency (cd/A)	a	38.0	30.6	35.3
	b	33.6	27.6	28.5
power efficiency (lm/W)	a	35.8	24.8	30.4
	b	21.6	15.9	18.2
V_{on} (V)	c	3.5	3.8	3.8
V_{100} (V)	b	4.9	5.5	5.0
max. luminance (cd/m^2) (voltage (V))		15 583	5840	17 625
		(15.8)	(15.0)	(14.6)
CIE1931 coordinates	b	(0.190, 0.328)	(0.178, 0.285)	(0.308, 0.344)
	d	(0.189, 0.322)	(0.181, 0.286)	(0.328, 0.343)
	e	(0.211, 0.331)		(0.330, 0.342)

[a]Maximum efficiency. [b]Recorded at 1×10^2 cd/m^2; [c]Turn-on voltage measured at 1 cd/m^2; [d]Measured at 1×10^3 cd/m^2; [e]Measured at 1×10^4 cd/m^2.

Figure 6 and Table 3 show the electroluminescence (EL) characteristics and associated numerical data. As revealed in the EL spectra (Figure 6a), the effective energy transfer between the host and guest renders the sky-blue emission for both devices A and B. Note that the first EL band at 454−461 nm has gained in intensity versus that of the photoluminescent (PL) spectra showed in Figure 2. The slight variation of related intensity between emission vibronic peaks is likely resulting from the optical interference.[89,90] No additional emission peak was observed in the EL spectra, implying that the carrier recombination zone is located within the EML and that the exciton diffusion to the adjacent layers has been avoided. The emission colors of both devices are stable within in a wide luminance range of 1 to 1×10^3 cd/m^2, showing excellent control of device properties. The CIE coordinates of devices A and B at a luminance of 100 cd/m^2 are recorded to be (0.190, 0.328) and (0.178, 0.285), respectively. In general, incorporating thermally unstable iridium complexes causes the breakdown of blue PhOLEDs upon swift increase of voltage. Fortunately, this inferiority did not appear in our devices, reaffirming adequate thermal stability of these new complexes.

From the current density−voltage-luminance ($J−V−L$) curves, devices A and B exhibit the turn-on voltage of 3.5 and 3.8 V, respectively. The operating voltages were then increased to 4.9 V for device A and 5.5 V for device B at the luminance of 1×10^2 cd/m^2. The electrical properties shown here are superior to many reported blue-emitting Ir(III) phosphors,[75,78,91] leading us to believe that the bipolar transport ability of mCP and the improved architecture design are two major factors for the reduction of the operating voltages. Moreover, device A achieved a maximum luminance of 15583 cd/m^2 at 15.8 V, whereas device B had a peak luminance of 5804 cd/m^2 at an operating voltage of 15.0 V. As predicted, higher luminance was achieved in A because of the slightly lower gap and the outstanding PL quantum yield of complex **2**.

In terms of efficiency characteristics, device A exhibited peak EL efficiencies of up to 17.9%, 38.0 cd/A, and 35.8 lm/W upon application of a forward bias. At a practical brightness of 10^2 cd/m^2, the recorded efficiencies were 15.8%, 33.6 cd/A, and 21.6 lm/W, respectively. Similarly, device B (i.e., with phosphor **4**) exhibited peak efficiencies of 15.5%, 30.6 cd/A, and 24.8 lm/W, and at a practical brightness of 10^2 cd/m^2, the efficiency remained at around 14.0%, 27.6 cd/A, and 15.9 lm/W. The recorded efficiency of device B is slightly inferior to that of device A, the result of which can be ascribed to the lower quantum yield of **4**. The high external quantum efficiencies of devices imply a high internal quantum efficiency of nearly 90% in both devices.[92] In view of the energy-level relationship, the holes are expected to be blocked at the TAPC/mCP interface, thereby deterring hole transport and suppressing excessive hole injection into the emitting region. Based on this result, an optimal carrier and exciton balance was achieved. Consequently, the double ECLs configuration has effectively restrained the exciton formation and recombination at both EMLs.

Moreover, triplet−triplet annihilation (TTA) is known to be a potential problem for phosphorescent OLEDs.[93−95] Fortunately, the degree of TTA in the current devices seems to be less severe, especially in device A. On a closer inspection of the efficiency roll-off, one can see that the external quantum efficiency reaches 13.4% at a higher luminance of 1×10^3 cd/m^2 in A, which was sustained at about 75% of the peak

efficiency. We thus conclude that the bipolar transport property of mCP could provide an enlarged space for carrier recombination and then further relax the excitons in the condensed phase.

Encouraged by the aforementioned device performances, we made further attempts to attain efficient white OLEDs (WOLEDs) based on the architecture of device A. On this basis, the red emitting $[Os(bpftz)_2(PPh_2Me)_2]$ (**5**)[96] seems to provide a good complementary color with respect to the sky-blue emission of **2** and was thus selected for fabrication of the WOLEDs.[97,98] Essentially, the location and concentration of dopant **5** are crucial in influencing the apparent color and carrier balance. Aiming at stabilizing the emission colors, we doped the Os(II) phosphor **5** at the mCP/UGH2 interface in EML1, which is the principal exciton formation zone, to ensure ample red emission.[99] Furthermore, to mitigate the carrier imbalance, which might be caused by the carrier trapping, we restricted the thickness of this Os(II) layer to 1 nm. Thus, the architecture of WOLEDs (i.e., device C) is illustrated as: ITO (110 nm)/TAPC (30 nm)/mCP (3 nm)/mCP doped with 6.0 wt.% **2** (24 nm)/mCP doped with x wt.% **5** (1 nm)/UGH2 doped with 6.0 wt % **2** (3 nm)/UGH2 (2 nm)/TmPyPB (50 nm)/LiF (0.8 nm)/Al (150 nm) (cf. Figure 5). Through optimizing the doping concentration, the pure-white emission was obtained by using 5 wt % **5**.

The resulting EL characteristics of device C are shown in Figure 6b−f. From the normalized EL spectra at various luminance, device C exhibited a stable white emission with CIE$_{x,y}$ coordinates close to the equal-energy white point. The intensity of red emission increased slightly at higher voltage, implying that the energy transferred from **2** to the Os(II) dopant **5** rose with increasing operation voltages. Fortunately, its small thickness has effectively reduced the unwanted energy transfer. All EL spectra were essentially identical with luminance between 10^3 and 10^4 cd/m^2, which exhibit the CIE$_{x,y}$ coordinates of 0.33, 0.34 and color variation (Δx, Δy) of 0.022, 0.002. For book keeping, the color rendering index (CRI) and the correlated color temperature (CCT) were estimated to be 69 and 5710 K at luminance of 1×10^3 cd/m^2, respectively.

More information can be deduced by comparing the $J−V−L$ plots of both devices A and C. It is believed that the red Os(II) dopant primarily causes carrier trapping; thus the driving voltage of device C did not increase significantly as compared to that of A. The introduction of this red-emitting layer merely boosted the turn-on voltage by 0.3 V. Even at a practical luminance of 1×10^2 cd/m^2, the driving voltage of device C was maintained at as low as 5 V, showing the reduction of the trapping phenomenon. The maximum luminance of device C was then recorded to be 17625 cd/m^2 at 14.6 V. This increased luminance over that of device A maybe attributed to the increased contribution from longer wavelength emission in the EL spectrum. The optimal carrier balance was the result of its sufficient transport ability as well as its superior architecture design. Furthermore, the peak efficiencies of device C went up to 17.3%, 35.3 cd/A, and 30.4 lm/W (see Table 2), whereas at a practical brightness of 1×10^2 cd/m^2, the efficiencies were still maintained at the higher levels of 14.6%, 28.5 cd/A, and 18.2 lm/W, confirming the superiority of **2** as a blue emitter in developing all phosphorescent WOLEDs.

■ CONCLUSION

In summary, a new series of sky blue-emitting Ir(III) phosphors assembled using fluorine-free pyridyl pyrimidine chromophores were synthesized and characterized. With this new phosphor design, the phosphorescent OLEDs employing Ir(III) complex **2** exhibited a peak external quantum efficiency of 17.9%, a luminance efficiency (LE) of 38.0 cd/A, and a power efficiency (PE) of 35.8 lm/W, confirming their superior device characteristics. Furthermore, through combination of sky blue Ir(III) phosphor **2** and red Os(II) dopant **5**, we also successfully fabricated the all phosphorescent WOLEDs to further validate the proposed strategy of stabilized emission without compromising performance. Comprehensive device analysis indicated that the restricted thickness of the red emitting layer (localized at the exciton formation zone) has effectively mitigated color variation (Δx, Δy) in the CIE coordinates, which was measured to be only (0.022, 0.002) for luminance between 1×10^2 and 1×10^4 cd/m^2. Furthermore, the maximum efficiencies of WOLEDs were 17.3%, 35.3 cd/A, and 30.4 lm/W. The lower operation voltages and outstanding device performances demonstrate the great potential of these sky blue Ir(III) phosphors for use in the emerging display and lighting applications.

■ AUTHOR INFORMATION

Corresponding Author

*E-mail: chc@saturn.yzu.edu.tw (C.-H.C.); ychi@mx.nthu.edu.tw (Y.C.); chop@ntu.edu.tw (P.-T.C.).

Notes

The authors declare no competing financial interest.

■ ACKNOWLEDGMENTS

■ REFERENCES

(1) So, F.; Kido, J.; Burrows, P. *MRS Bull.* **2008**, *33*, 663−669.

(2) Thompson, M. E. *MRS Bull.* **2007**, *32*, 694−701.

(3) Williams, J. A. G.; Develay, S.; Rochester, D. L.; Murphy, L. *Coord. Chem. Rev.* **2008**, *252*, 2596−2611.

(4) Wong, W.-Y.; Ho, C.-L. *J. Mater. Chem.* **2009**, *19*, 4457−4482.

(5) Wong, W. -Y.; Ho, C. -L. *Coord. Chem. Rev.* **2009**, *253*, 1709−1758.

(6) Chen, Z.-Q.; Bian, Z.-Q.; Huang, C.-H. *Adv. Mater.* **2010**, *22*, 1534−1539.

(7) Zhou, G.; Wong, W.-Y.; Suo, S. *J. Photochem. Photobiol. C* **2010**, *11*, 133−156.

(8) Chaskar, A.; Chen, H.-F.; Wong, K.-T. *Adv. Mater.* **2011**, *23*, 3876−3895.

(9) Farinola, G. M.; Ragni, R. *Chem. Soc. Rev.* **2011**, *40*, 3467−3482.

(10) Sasabe, H.; Kido, J. *Chem. Mater.* **2011**, *23*, 621−630.

(11) Xiao, L.; Chen, Z.; Qu, B.; Luo, J.; Kong, S.; Gong, Q.; Kido, J. *Adv. Mater.* **2011**, *23*, 926−952.

(12) Zhou, G.; Wong, W.-Y.; Yang, X. *Chem. Asian J.* **2011**, *6*, 1706−1727.

(13) Zhu, X.-H.; Peng, J.; Cao, Y.; Roncali, J. *Chem. Soc. Rev.* **2011**, *40*, 3509−3524.

(14) Zuniga, C. A.; Barlow, S.; Marder, S. R. *Chem. Mater.* **2011**, *23*, 658−681.

(15) Yook, K. S.; Lee, J. Y. *Adv. Mater.* **2012**, *24*, 3169−3190.

(16) You, Y.; Nam, W. *Chem. Soc. Rev.* **2012**, *41*, 7061−7084.

(17) Ho, C. -L.; Wong, W. -Y. *Coord. Chem. Rev.* **2013**, *257*, 1614−1649.

(18) Fu, H.; Cheng, Y.-M.; Chou, P.-T.; Chi, Y. *Mater. Today* **2011**, *14*, 472−479.

(19) Ho, C. -L.; Wong, W. -Y. *New J. Chem.* **2013**, *37*, 1665−1683.

(20) Lamansky, S.; Djurovich, P.; Murphy, D.; Abdel-Razzaq, F.; Kwong, R.; Tsyba, I.; Bortz, M.; Mui, B.; Bau, R.; Thompson, M. E. *Inorg. Chem.* **2001**, *40*, 1704−1711.

(21) Li, J.; Djurovich, P. I.; Alleyne, B. D.; Tsyba, I.; Ho, N. N.; Bau, R.; Thompson, M. E. *Polyhedron* **2004**, *23*, 419−428.

(22) Coppo, P.; Plummer, E. A.; De Cola, L. *Chem. Commun.* **2004**, 1774−1775.

(23) Yeh, S.-J.; Wu, M.-F.; Chen, C.-T.; Song, Y.-H.; Chi, Y.; Ho, M.-H.; Hsu, S.-F.; Chen, C. H. *Adv. Mater.* **2005**, *17*, 285−289.

(24) Seo, H.-J.; Yoo, K.-M.; Song, M.; Park, J. S.; Jin, S.-H.; Kim, Y. I.; Kim, J.-J. *Org. Electron.* **2010**, *11*, 564−572.

(25) Liu, Y.; Gahungu, G.; Sun, X.; Su, J.; Qu, X.; Wu, Z. *Dalton Trans.* **2012**, *41*, 7595−7603.

(26) Chen, L.; You, H.; Yang, C.; Ma, D.; Qin, J. *Chem. Commun.* **2007**, 1352−1354.

(27) Zhu, Y.-C.; Zhou, L.; Li, H.-Y.; Xu, Q.-L.; Teng, M.-Y.; Zheng, Y.-X.; Zuo, J.-L.; Zhang, H.-J.; You, X.-Z. *Adv. Mater.* **2011**, *23*, 4041−4046.

(28) Chiu, Y.-C.; Hung, J.-Y.; Chi, Y.; Chen, C.-C.; Chang, C.-H.; Wu, C.-C.; Cheng, Y.-M.; Yu, Y.-C.; Lee, G.-H.; Chou, P.-T. *Adv. Mater.* **2009**, *21*, 2221−2225.

(29) Hung, J.-Y.; Chi, Y.; Pai, I.-H.; Cheng, Y.-M.; Yu, Y.-C.; Lee, G.-H.; Chou, P.-T.; Wong, K.-T.; Chen, C.-C.; Wu, C.-C. *Dalton Trans.* **2009**, 6472−6475.

(30) Chiu, Y.-C.; Lin, C.-H.; Hung, J.-Y.; Chi, Y.; Cheng, Y.-M.; Wang, K.-W.; Chung, M.-W.; Lee, G.-H.; Chou, P.-T. *Inorg. Chem.* **2009**, *48*, 8164−8172.

(31) Chiu, Y.-C.; Chi, Y.; Hung, J.-Y.; Cheng, Y.-M.; Yu, Y.-C.; Chung, M.-W.; Lee, G.-H.; Chou, P.-T.; Chen, C.-C.; Wu, C.-C.; Hsieh, H.-Y. *ACS Appl. Mater. Interfaces* **2009**, *1*, 433−442.

(32) Yang, C.-H.; Li, S.-W.; Chi, Y.; Cheng, Y.-M.; Yeh, Y.-S.; Chou, P.-T.; Lee, G.-H.; Wang, C.-H.; Shu, C.-F. *Inorg. Chem.* **2005**, *44*, 7770−7780.

(33) Baranoff, E.; Fantacci, S.; De Angelis, F.; Zhang, X.; Scopelliti, R.; Gratzel, M.; Nazeeruddin, M. K. *Inorg. Chem.* **2011**, *50*, 451−462.

(34) Lo, S.-C.; Shipley, C. P.; Bera, R. N.; Harding, R. E.; Cowley, A. R.; Burn, P. L.; Samuel, I. D. W. *Chem. Mater.* **2006**, *18*, 5119−5129.

(35) Yook, K. S.; Jeon, S. O.; Joo, C. W.; Lee, J. Y. *Org. Electron.* **2009**, *10*, 170−173.

(36) Fan, C.; Li, Y.; Yang, C.; Wu, H.; Qin, J.; Cao, Y. *Chem. Mater.* **2012**, *24*, 4581−4587.

(37) Jung, N.; Lee, E.; Kim, J.; Park, H.; Park, K.-M.; Kang, Y. *Bull. Korean Chem. Soc.* **2012**, *33*, 183−188.

(38) Lee, S. J.; Park, K.-M.; Yang, K.; Kang, Y. *Inorg. Chem.* **2009**, *48*, 1030−1037.

(39) Beyer, B.; Ulbricht, C.; Escudero, D.; Friebe, C.; Winter, A.; Gonzalez, L.; Schubert, U. S. *Organometallics* **2009**, *28*, 5478−5488.

(40) Sivasubramaniam, V.; Brodkorb, F.; Hanning, S.; Loebl, H. P.; van Elsbergen, V.; Boerner, H.; Scherf, U.; Kreyenschmidt, M. *J. Fluorine Chem.* **2009**, *130*, 640−649.

(41) Zheng, Y.; Batsanov, A. S.; Edkins, R. M.; Beeby, A.; Bryce, M. R. *Inorg. Chem.* **2012**, *51*, 290−297.

(42) Nierengarten, H.; Rojo, J.; Leize, E.; Lehn, J.-M.; Van Dorsselaer, A. *Eur. J. Inorg. Chem.* **2002**, 573−579.

(43) Cuperly, D.; Gros, P.; Fort, Y. *J. Org. Chem.* **2002**, *67*, 238−241.

(44) Wu, K.-L.; Ku, W.-P.; Clifford, J. N.; Palomares, E.; Ho, S.-T.; Chi, Y.; Liu, S.-H.; Chou, P.-T.; Nazeeruddin, M. K.; Grätzel, M. *Energy Environ. Sci.* **2013**, *6*, 859−870.

(45) Sheldrick, G. M. *Acta Crystallogr., Sect. A* **2008**, *64*, 112−122.

(46) Chou, P.-T.; Yu, W.-S.; Cheng, Y.-M.; Pu, S.-C.; Yu, Y.-C.; Lin, Y.-C.; Huang, C.-H.; Chen, C.-T. *J. Phys. Chem. A* **2004**, *108*, 6487−6498.

(47) Chen, J.-L.; Chi, Y.; Chen, K.; Cheng, Y.-M.; Chung, M.-W.; Yu, Y.-C.; Lee, G.-H.; Chou, P.-T.; Shu, C.-F. *Inorg. Chem.* **2010**, *49*, 823–832.

(48) Hay, P. J.; Wadt, W. R. *J. Chem. Phys.* **1985**, *82*, 270–283.

(49) Ait-Haddou, H.; Bejan, E.; Daran, J.-C.; Balavoine, G. G. A.; Berruyer-Penaud, F.; Bonazzola, L.; Smaoui-Chaabouni, H.; Amouyal, E. *J. Chem. Soc., Dalton Trans.* **1999**, 3095–3101.

(50) Lowry, M. S.; Hudson, W. R.; Pascal, R. A., Jr.; Bernhard, S. *J. Am. Chem. Soc.* **2004**, *126*, 14129–14135.

(51) Du, B.; Wang, L.; Wu, H.; Yang, W.; Zhang, Y.; Liu, R.; Sun, M.; Peng, J.; Cao, Y. *Chem.—Eur. J.* **2007**, *13*, 7432–7442.

(52) Peng, T.; Yang, Y.; Liu, Y.; Ma, D.; Hou, Z.; Wang, Y. *Chem. Commun.* **2011**, *47*, 3150–3152.

(53) Baranoff, E.; Jung, I.; Scopelliti, R.; Solari, E.; Graetzel, M.; Nazeeruddin, M. K. *Dalton Trans.* **2011**, *40*, 6860–6867.

(54) Lin, C.-H.; Chiu, Y.-C.; Chi, Y.; Tao, Y.-T.; Liao, L.-S.; Tseng, M.-R.; Lee, G.-H. *Organometallics* **2012**, *31*, 4349–4355.

(55) Tamayo, A. B.; Alleyne, B. D.; Djurovich, P. I.; Lamansky, S.; Tsyba, I.; Ho, N. N.; Bau, R.; Thompson, M. E. *J. Am. Chem. Soc.* **2003**, *125*, 7377–7387.

(56) Ho, C. -L.; Wong, W. -Y.; Gao, Z. -Q.; Chen, C. -H.; Cheah, K. -W.; Yao, B.; Xie, Z.; Wang, Q.; Ma, D.; Wang, L.; Yu, X. -M.; Kwok, H. -S.; Lin, Z. *Adv. Funct. Mater.* **2008**, *18*, 319–331.

(57) Ho, C. -L.; Wong, W. -Y.; Wang, Q.; Ma, D.; Wang, L.; Lin, Z. *Adv. Funct. Mater.* **2008**, *18*, 928–937.

(58) Lee, T.-C.; Chang, C.-F.; Chiu, Y.-C.; Chi, Y.; Chan, T.-Y.; Cheng, Y.-M.; Lai, C.-H.; Chou, P.-T.; Lee, G.-H.; Chien, C.-H.; Shu, C.-F.; Leonhardt, J. *Chem. Asian J.* **2009**, *4*, 742–753.

(59) Zhou, G.-J.; Wang, Q.; Wong, W.-Y.; Ma, D.; Wang, L.; Lin, Z. *J. Mater. Chem.* **2009**, *19*, 1872–1883.

(60) Kim, C. Y.; Ha, D.-G.; Kang, H. H.; Yun, H.-J.; Kwon, S.-K.; Kim, J.-J.; Kim, Y.-H. *J. Mater. Chem.* **2012**, *22*, 22721–22726.

(61) Zhou, Y.; Li, W.; Liu, Y.; Zeng, L.; Su, W.; Zhou, M. *Dalton Trans.* **2012**, *41*, 9373–9381.

(62) Zhang, F.; Wang, L.; Chang, S.-H.; Huang, K.-L.; Chi, Y.; Hung, W.-Y.; Chen, C.-M.; Lee, G.-H.; Chou, P.-T. *Dalton Trans.* **2013**, *42*, 7111–7119.

(63) Xu, M.; Zhou, R.; Wang, G.; Xiao, Q.; Du, W.; Che, G. *Inorg. Chim. Acta* **2008**, *361*, 2407–2412.

(64) Stagni, S.; Colella, S.; Palazzi, A.; Valenti, G.; Zacchini, S.; Paolucci, F.; Marcaccio, M.; Albuquerque, R. Q.; De Cola, L. *Inorg. Chem.* **2008**, *47*, 10509–10521.

(65) Yang, C.-H.; Mauro, M.; Polo, F.; Watanabe, S.; Muenster, I.; Frohlich, R.; De Cola, L. *Chem. Mater.* **2012**, *24*, 3684–3695.

(66) Kessler, F.; Watanabe, Y.; Sasabe, H.; Katagiri, H.; Nazeeruddin, M. K.; Graetzel, M.; Kido, J. *J. Mater. Chem. C* **2013**, *1*, 1070–1075.

(67) Lowry, M. S.; Bernhard, S. *Chem.—Eur. J.* **2006**, *12*, 7970–7977.

(68) Ren, X.; Giesen, D. J.; Rajeswaran, M.; Madaras, M. *Organometallics* **2009**, *28*, 6079–6089.

(69) Hallett, A. J.; Kariuki, B. M.; Pope, S. J. A. *Dalton Trans.* **2011**, *40*, 9474–9481.

(70) Wang, R.; Deng, L.; Zhang, T.; Li, J. *Dalton Trans.* **2012**, *41*, 6833–6841.

(71) Swanick, K. N.; Ladouceur, S.; Zysman-Colman, E.; Ding, Z. *Chem. Commun.* **2012**, *48*, 3179–3181.

(72) Tsai, M.-H.; Hong, Y.-H.; Chang, C.-H.; Su, H.-C.; Wu, C.-C.; Matoliukstyte, A.; Simokaitiene, J.; Grigalevicius, S.; Grazulevicius, J. V.; Hsu, C.-P. *Adv. Mater.* **2007**, *19*, 862–866.

(73) Yang, C.-H.; Cheng, Y.-M.; Chi, Y.; Hsu, C.-J.; Fang, F.-C.; Wong, K.-T.; Chou, P.-T.; Chang, C.-H.; Tsai, M.-H.; Wu, C.-C. *Angew. Chem., Int. Ed.* **2007**, *46*, 2418–2421.

(74) Chang, C.-F.; Cheng, Y.-M.; Chi, Y.; Chiu, Y.-C.; Lin, C.-C.; Lee, G.-H.; Chou, P.-T.; Chen, C.-C.; Chang, C.-H.; Wu, C.-C. *Angew. Chem., Int. Ed.* **2008**, *47*, 4542–4545.

(75) Lin, C.-H.; Chang, Y.-Y.; Hung, J.-Y.; Lin, C.-Y.; Chi, Y.; Chung, M.-W.; Lin, C.-L.; Chou, P.-T.; Lee, G.-H.; Chang, C.-H.; Lin, W.-C. *Angew. Chem., Int. Ed.* **2011**, *50*, 3182–3186.

(76) Burin, A. L.; Ratner, M. A. *J. Phys. Chem. A* **2000**, *104*, 4704–4710.

(77) Holmes, R. J.; Forrest, S. R.; Tung, Y.-J.; Kwong, R. C.; Brown, J. J.; Garon, S.; Thompson, M. E. *Appl. Phys. Lett.* **2003**, *82*, 2422–3.

(78) Eom, S.-H.; Zheng, Y.; Chopra, N.; Lee, J.; So, F.; Xue, J. *Appl. Phys. Lett.* **2008**, *93*, 133309–3.

(79) Holmes, R. J.; D'Andrade, B. W.; Forrest, S. R.; Ren, X.; Li, J.; Thompson, M. E. *Appl. Phys. Lett.* **2003**, *83*, 3818–3.

(80) Ren, X.; Li, J.; Holmes, R. J.; Djurovich, P. I.; Forrest, S. R.; Thompson, M. E. *Chem. Mater.* **2004**, *16*, 4743–4747.

(81) Tsuboi, T.; Liu, S.-W.; Wu, M.-F.; Chen, C.-T. *Org. Electron.* **2009**, *10*, 1372–1377.

(82) Fukagawa, H.; Watanabe, K.; Tsuzuki, T.; Tokito, S. *Appl. Phys. Lett.* **2008**, *93*, 133312–3.

(83) Goushi, K.; Kwong, R.; Brown, J. J.; Sasabe, H.; Adachi, C. *J. Appl. Phys.* **2004**, *95*, 7798–7802.

(84) Chopra, N.; Lee, J.; Zheng, Y.; Eom, S.-H.; Xue, J.; So, F. *Appl. Phys. Lett.* **2008**, *93*, 143307–3.

(85) Su, S.-J.; Chiba, T.; Takeda, T.; Kido, J. *Adv. Mater.* **2008**, *20*, 2125–2130.

(86) Chang, C.-H.; Kuo, M.-C.; Lin, W.-C.; Chen, Y.-T.; Wong, K.-T.; Chou, S.-H.; Mondal, E.; Kwong, R. C.; Xia, S.; Nakagawa, T.; Adachi, C. *J. Mater. Chem.* **2012**, *22*, 3832–3838.

(87) Chang, C.-H.; Chen, C.-C.; Wu, C.-C.; Yang, C.-H.; Chi, Y. *Org. Electron.* **2009**, *10*, 1364–1371.

(88) Hung, W.-Y.; Chen, Z.-W.; You, H.-W.; Fan, F.-C.; Chen, H.-F.; Wong, K.-T. *Org. Electron.* **2011**, *12*, 575–581.

(89) Wu, C.-C.; Chen, C.-W.; Lin, C.-L.; Yang, C.-J. *J. Disp. Technol.* **2005**, *1*, 248–266.

(90) Lin, C.-L.; Lin, H.-W.; Wu, C.-C. *Appl. Phys. Lett.* **2005**, *87*, 021101–3.

(91) Park, M. S.; Lee, J. Y. *Chem. Mater.* **2011**, *23*, 4338–4343.

(92) Bulovie, V.; Khalfin, V. B.; Gu, G.; Burrows, P. E.; Garbuzov, D. Z.; Forrest, S. R. *Phys. Rev. B* **1998**, *58*, 3730–3740.

(93) Baldo, M. A.; O'Brien, D. F.; You, Y.; Shoustikov, A.; Sibley, S.; Thompson, M. E.; Forrest, S. R. *Nature* **1998**, *395*, 151–154.

(94) Baldo, M. A.; Adachi, C.; Forrest, S. R. *Phys. Rev. B* **2000**, *62*, 10967–10977.

(95) Zhou, G. -J.; Wong, W. -Y.; Yao, B.; Xie, Z.; Wang, L. *J. Mater. Chem.* **2008**, *18*, 1799–1809.

(96) Wu, C.-H.; Shih, P.-I.; Shu, C.-F.; Chi, Y. *Appl. Phys. Lett.* **2008**, *92*, 233303–3.

(97) Chang, C.-H.; Lin, Y.-H.; Chen, C.-C.; Chang, C.-K.; Wu, C.-C.; Chen, L.-S.; Wu, W.-W.; Chi, Y. *Org. Electron.* **2009**, *10*, 1235–1240.

(98) Chang, C.-H.; Chen, C.-C.; Wu, C.-C.; Chang, S.-Y.; Hung, J.-Y.; Chi, Y. *Org. Electron.* **2010**, *11*, 266–272.

(99) Chang, C.-H.; Tien, K.-C.; Chen, C.-C.; Lin, M.-S.; Cheng, H.-C.; Liu, S.-H.; Wu, C.-C.; Hung, J.-Y.; Chiu, Y.-C.; Chi, Y. *Org. Electron.* **2010**, *11*, 412–418.